COMMUNICATIONS PHYSICS

ARTICLE

Dynamically tuned non-classical light emission from atomic defects in hexagonal boron nitride

Snežana Lazić[1], André Espinha [1], Sergio Pinilla Yanguas[1], Carlos Gibaja[2], Félix Zamora [2], Pablo Ares [3], Manish Chhowalla[4], Wendel S. Paz[5], Juan José Palacios Burgos [3], Alberto Hernández-Mínguez [6], Paulo V. Santos[6] & Herko P. van der Meulen [1]

Luminescent defects in hexagonal boron nitride (h-BN) have recently emerged as a promising platform for non-classical light emission. On-chip solutions, however, require techniques for controllable in-situ manipulation of quantum light. Here, we demonstrate the dynamic spectral and temporal tuning of the optical emission from h-BN via moving acousto-mechanical modulation induced by stimulated phonons. When perturbed by the propagating acoustic phonon, the optically probed radiative h-BN defects are periodically strained and their sharp emission lines are modulated by the deformation potential coupling. This results in an acoustically driven spectral tuning within a 2.5-meV bandwidth. Our findings, supported by first-principles theoretical calculations, reveal exceptionally high elasto-optic coupling in h-BN of ~50 meV/%. Temporal control of the emitted photons is achieved by combining the acoustically mediated fine-spectral tuning with spectral detection filtering. This study opens the door to the use of sound for scalable integration of h-BN emitters in nanophotonic and quantum information technologies.

[1] Departamento de Física de Materiales, Instituto Universitario de Ciencia de Materiales "Nicolás Cabrera" (INC) and Condensed Matter Physics Center (IFIMAC), Universidad Autónoma de Madrid (UAM), 28049 Madrid, Spain. [2] Departamento de Química Inorgánica and IFIMAC, Universidad Autónoma de Madrid (UAM), 28049 Madrid, Spain. [3] Departamento de Física de la Materia Condensada, INC and IFIMAC, Universidad Autónoma de Madrid (UAM), 28049 Madrid, Spain. [4] Department of Materials Science and Metallurgy, University of Cambridge, Cambridge CB3 0FS, UK. [5] Instituto de Física, Universidade Federal do Rio de Janeiro, Caixa Postal 68528, Rio de Janeiro, RJ 21941-972, Brazil. [6] Paul-Drude-Institut für Festkörperelektronik, Leibniz-Institut im Forschungsverbund Berlin e.V., Hausvogteiplatz 5–7, 10117 Berlin, Germany. Correspondence and requests for materials should be addressed to S.L. (email: lazic.snezana@uam.es)

Owing to their unique mechanical, electronic and optical properties, a number of two-dimensional van der Waals layered materials, including semiconducting transition metal dichalcogenides and insulating hexagonal boron nitride (h-BN), have emerged as promising candidates for room temperature-quantum photonics. In particular, deterministic generation and manipulation of light at the fundamental single-photon limit play an essential role in a variety of applications using photonic qubits that go beyond the capabilities of today's classical-information-based technologies, including quantum communications and quantum computing[1,2].

The atom-like deep-level defects in h-BN have recently emerged as prominent candidates for single-photon emission. Although their microscopic nature is still under debate, these luminescent centers have been proven to be extremely robust, high-temperature, linearly polarized and ultra-bright sources of non-classical (i.e., antibunched) light[3–13]. The prominence of single-photon emitters (SPEs) in h-BN is, however, hindered by the emitter-to-emitter wavelength variability, which covers a broad range in the visible and near-infrared spectrum[6,7,9–13]. Recent theoretical and experimental analyses reported in refs. [6,7,9] suggest that this wide span of the emission wavelengths may result from inhomogeneous broadening of several defect species or can likely originate from defects belonging to the same atomistic model coupled to the fluctuating local lattice strain and/or dielectric environments. Whatever its origin, such large spectral inhomogeneity has shown to be detrimental to developing identical single-photon sources, as well as for other applications in nanophotonics and quantum information processing that rely on a strict and well-defined emission energy. To this end, current proposals for scalable (i.e., on-chip) quantum technologies require photonic sources with controllable optoelectronic properties. To date, manipulation of light emitted from h-BN defect states has only been experimentally demonstrated by tuning the photon emission energy using either static strain[6,7] or electric field[14]. One way to achieve this dynamically is via the acousto-mechanical and acousto-electric effects induced by radio frequency (RF) surface acoustic waves (SAWs). As previously reported for other material systems, the oscillating strain and piezoelectric fields of the propagating sound wave can efficiently couple to defect centers[15–17] or other nanostructures, such as semiconductor quantum dots (QDs)[18–23], placed close to the surface of the wave-carrying medium.

In this work, we report on the in situ control of the optical emission originating from atom-like defects in h-BN using SAWs. We show that, when subjected to the SAW-induced acousto-mechanical coupling, the emission energy of individual defect-related linearly polarized SPEs is periodically modulated. The magnitude of this modulation depends on the mechanical coupling strength between the emitting state and the acoustic substrate. From the optical response of the emitting states to the moving mechanical vibration, we estimate the absolute deformation potential and the strain-induced tuning coefficient for h-BN to be ~5 eV and ~50 meV/%, respectively. These values, which are also substantiated by theoretical analysis, exceed by an order of magnitude the previous experimental findings obtained under externally applied static strain[6], thereby evidencing high elasto-optic coupling in h-BN. The here reported strain-mediated real-time control of the emission energy of individual atomic defects is further combined with spectral detection filtering for temporal control of the emitted photons. Our results, therefore, demonstrate that SAWs provide a particularly powerful external method for "wireless" and non-destructive strain engineering, allowing for simultaneous fine-spectral tunability and time-gated emission of single photons. These functionalities are beneficial for the deployment of h-BN defect centers in quantum and integrated photonic applications.
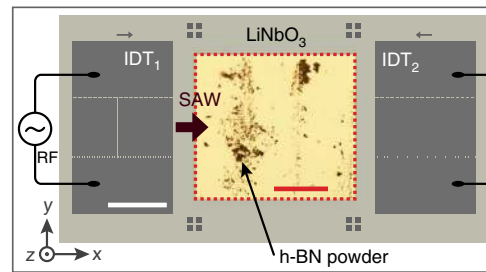

Fig. 1 Schematics of the surface acoustic wave (SAW) chip for spectroscopic measurement. Hexagonal boron nitride (h-BN) powder is dispersed on the SAW path defined by a pair of interdigital transducers (IDTs, scale bar = 400 μm) lithographically patterned on a lithium niobate (LiNbO₃) crystal. The x-axis of the laboratory reference frame corresponds to the SAW propagation direction. An optical microscope image of the dispersed h-BN powder (marked by a dotted red rectangle, scale bar = 50 μm) is superimposed on the chip layout

Results

Preparation and characterization of h-BN samples. The SAW experiments were performed using an acoustic delay line (depicted in Fig. 1) consisting of two interdigital transducers (IDTs) lithographically defined on the surface of a lithium niobate (LiNbO₃) crystal. The use of piezoelectric LiNbO₃ provides strong strain and piezoelectric fields along the SAW propagation direction and perpendicular to the substrate surface. The SAWs are electrically excited by applying an RF voltage to IDTs designed to operate at frequency f_{SAW} ~293 MHz at room temperature. The h-BN used in this study consists of commercially available powder in the form of grains with average diameter of around 1 μm (Sigma-Aldrich supplier). To produce SPEs, the h-BN powder was thermally expanded resulting in layers with lateral dimensions of ~200–300 nm and thickness of ~3–5 nm (see Supplementary Note 1), which were then mechanically dispersed onto the SAW propagation path (Fig. 1). Their photoluminescence (PL) was analyzed using a standard micro-PL experimental setup under direct optical illumination by a focused laser beam. Additional information on the acoustic delay line, sample fabrication and optical characterization is given in the Methods section.

Photo-physics of quantum light emitters. The representative low-temperature μ-PL spectrum in Fig. 2a recorded in the absence of the SAW reveals multiple characteristic zero-phonon lines (ZPLs), originating from bright and optically stable emitters contained within the laser-illuminated h-BN grains. Such narrow ZPLs have been seen frequently in h-BN layers and were attributed to the presence of point-like defects, which confine electronic levels deep within the band gap and act as recombination centers, resulting in non-classical light emission[2,6]. For each location on the sample, we observe a unique pattern of PL peaks spanning across a large spectral band of ~900 meV (Supplementary Note 2), in agreement with previous reports for h-BN flakes[6,7,11], powder[12] and epitaxially grown films[24]. We then performed a more detailed study of the photophysical properties of the PL peaks from Fig. 2a centered at 2.067, 2.090 and 2.155 eV (labeled ZPL₁, ZPL₂ and ZPL₃, respectively). The spectral position of these peaks coincides with the ZPLs previously measured in h-BN flakes[6–8,14].

The polarization-resolved micro-PL measurements in Fig. 2b show that these peaks are highly linearly polarized with an average polarization degree above 70%. Moreover, these as well as other lines appearing in the emission spectrum at different energies have their own intrinsic direction of polarization axes.
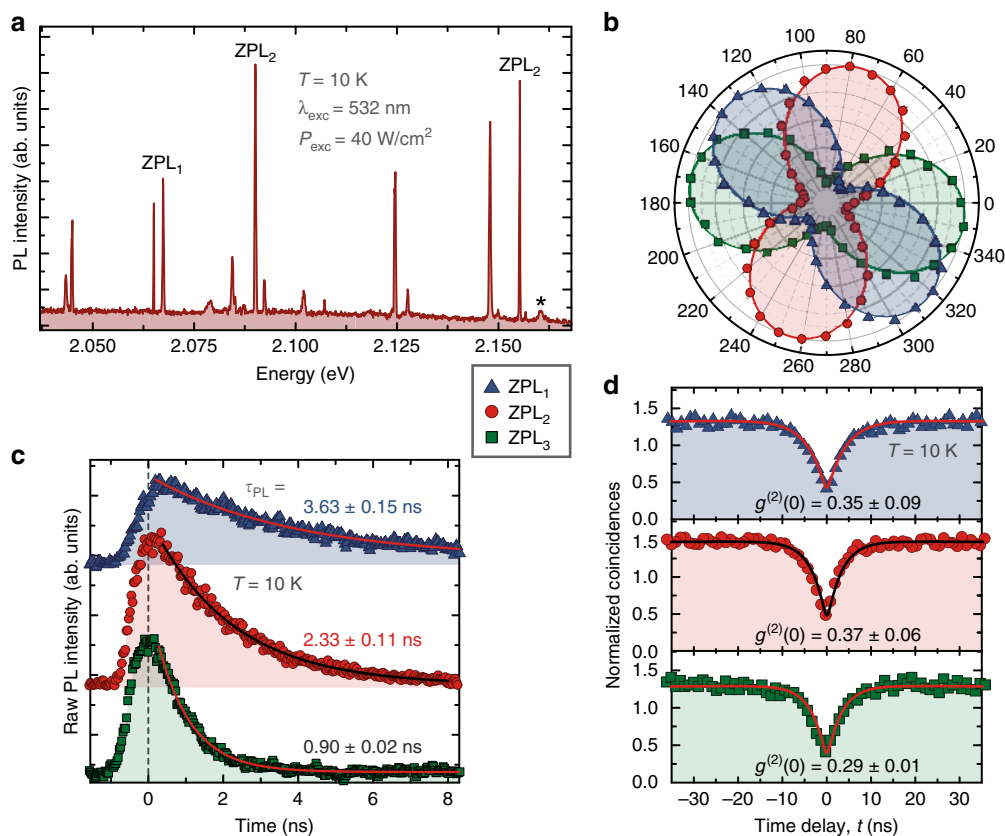
Fig. 2 Photo-physics of hexagonal boron nitride (h-BN) single-photon emitters. **a** A representative micro-photoluminescence spectrum excited with a 532 nm continuous-wave laser and recorded for the excitation power density of ~40 W/cm² at 10 K, showing multiple narrow zero-phonon emission lines (ZPLs). Peaks labeled ZPL_1, ZPL_2 and ZPL_3 are used in the experiments of **b**–**d**. The peak marked with asterisk corresponds to the E_{2g} Raman mode of h-BN[42]. **b** Normalized and background-corrected low-temperature intensities of peaks labeled ZPL_1 (blue triangles), ZPL_2 (red circles) and ZPL_3 (green squares) in **a** as a function of the polarization angle with respect to the SAW propagation direction (i.e., x-axis in Fig. 1) aligned at 0°. Solid traces are fits to a $\cos^2(\theta)$ function proving a high linear polarization degree of the emitted light. **c** Photoluminescence lifetime exhibiting excited-state time constants indicated in the figure, measured for the three signals in **b**. The decay curves are vertically offset for clarity. **d** Normalized second-order correlation function $g^{(2)}(\tau)$ of the same spectral lines as in **b** and **c** illustrating photon anti-bunching. Solid traces are theoretical fits of the experimental data obtained using Supplementary Eq. (1) in Supplementary Note 3. Measurements in **b** and **d** are acquired under the same laser excitation conditions as in **a**. The 442-nm laser pulses are used for **c**. The same color and symbol code is applied for all plots

This suggests that the linear polarization of the PL signal most likely originates from the particular anisotropic structure of the emission center[8,12].

The normalized luminescence decay curves of the three representative peaks are shown in Fig. 2c. The measured data (symbols) were fit using an exponential decay function (solid traces). The obtained lifetimes (τ_{PL} values outlined in Fig. 2c) are consistent with the characteristic decay times found in other monolayer and multilayer h-BN samples[7,8,10,13,25,26].

To demonstrate their quantized character, photon correlation statistics of the emitting states marked as ZPL_1, ZPL_2 and ZPL_3 in Fig. 2a was studied using a Hanbury Brown and Twiss (HBT) experimental setup (see Methods section). The three histograms in Fig. 2d were recorded under the same conditions as the PL spectrum in Fig. 2a. The suppression of the coincidence rate at zero time delay ($\tau = 0$) reflects the reduced probability of simultaneous multiple photon emission (i.e., photon anti-bunching). The residual counts at $\tau = 0$ are due to the background signal from the h-BN powder[12]. The single-photon performance was quantified by fitting the experimental data using a three-level system model[27], which has been typically used to describe single-photon emission in h-BN. According to this model, in addition to anti-bunching at a short timescale (tens of nanoseconds), our measurements also show a photon bunching

on much longer timescales (microsecond range, Supplementary Note 4), thereby indicating the presence of long-living site-specific metastable states[28]. The $g^{(2)}(0)$ values specified in Fig. 2d are estimated after taking into account the finite time resolution of the measurement setup and without any background correction (see Supplementary Note 3 for details). In fact, for all the investigated emission lines, the single-photon purity is below the 0.5 threshold, which is a characteristic signature of single-photon quantum emitters[1].

SAW-induced strain tuning of quantum emission. We then studied the control of the non-classical light emitted from the atomic-like defects in h-BN grains using SAWs. In Fig. 3a, we plot the three PL peaks from Fig. 2 recorded without an acoustic perturbation (upper traces) and perturbed by a 297.5 MHz (at 10 K) SAW (lower traces).

When the SAW is applied, the spectrum undergoes splitting of emission lines ZPL_2 and ZPL_3. The SAW-mediated spectral changes in Fig. 3a are dominated by the interaction between the emitting defects and the dynamic lattice deformations induced by the propagating SAW. In other words, as the SAW couples to the h-BN flake, the electronic energy levels of the embedded radiative defect are periodically shifted by the deformation potential coupling between the emitting state and the oscillating
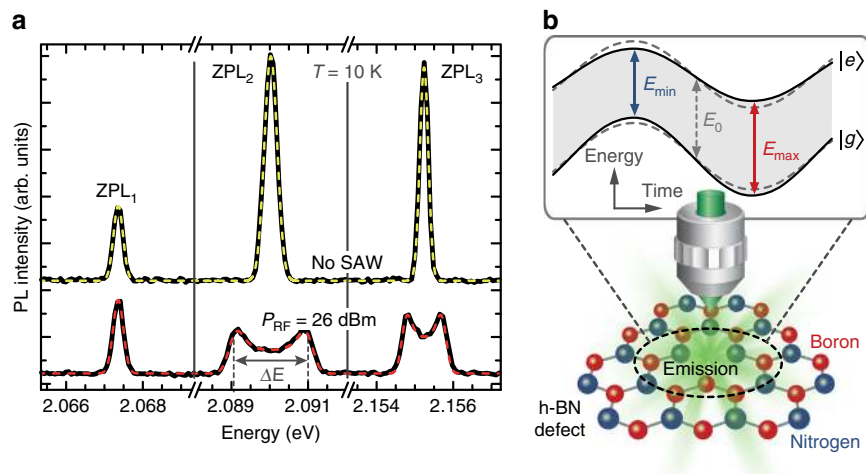
Fig. 3 Acoustically induced spectral changes. a Change in the zero-phonon line (ZPL) structure in low-temperature photoluminescence spectra of three hexagonal boron nitride (h-BN) defects in the presence of a surface acoustic wave (SAW): upper traces, no SAW present; lower traces, SAW generated by applying 26 dBm to the acoustic transducer. Spectra are vertically offset for clarity. Yellow and red dashed traces are fits to the experimental data of an unperturbed Gaussian peak and Eq. (1), respectively. **b** Simplified energy level diagram of the optically probed h-BN defect (denoted by the dashed black circle), showing an effect of the oscillating SAW strain on the defect's electronic structure. The optical transition energy between the excited state |e⟩ and the ground state |g⟩ is dynamically strain modulated around the ZPL energy E_0 with the amplitude of $\Delta E/2 = (E_{max} - E_{min})/2$, where E_{min} and E_{max} correspond to the minimum and maximum transition energies, respectively

SAW-driven mechanical vibration. The same result is observed when using the SAW propagating in the opposite direction (Fig. 1). The here reported acousto-mechanical effect is illustrated in Fig. 3b for the anti-site nitrogen vacancy defect (N_BV_N, comprising a missing nitrogen atom and a substitution of an adjacent boron atom by a nitrogen), which is one of the possible atomic structures yielding single-photon emission in the visible spectral range[6–8,14,29]. The figure depicts a schematic representation of the SAW-mediated time-varying tuning of the ZPL transition energy, for a simple case involving the excited state |e⟩ and a non-degenerate ground state |g⟩. Averaged over time, this modulation gives rise to an apparent splitting of the emission energies. Similar optical response to the acousto-mechanical contribution has been previously reported for quantum well[30,31] and QD[20,21,32–34] heterostructures in III–V semiconductors. In this context, the observed energy splitting reflects the difference between the transition energies at phases during the acoustic cycle corresponding to maximum compressive and tensile strain (marked with E_{max} and E_{min} in Fig. 3b, respectively).

For SAWs propagating on a strong piezoelectric medium (such as LiNbO₃), the mechanical wave is accompanied by an alternating piezoelectric field, which typically extends over a thickness approximately equal to one acoustic wavelength (i.e., a few micrometers) both below and above the substrate surface[33,34]. Contrary to the SAW strain field, which only acts on those defects exhibiting strong mechanical coupling to the substrate, the piezoelectric field is expected to have an effect on all emission dipoles located within its reach. Considering a random defect orientation, this field could also be responsible for the modulation of the emission lines in Fig. 3a. The spectral shifts associated with the quantum confined Stark effect governed by the SAW piezoelectric field acting in the direction out of the defect plane can be estimated by taking into account the Stark-induced tuning coefficients (as large as 5.4 nm per GV/m), determined experimentally for atomic defects in h-BN flakes under externally applied out-of-plane static electric fields[14]. The SAW-induced piezoelectric fields on the surface of a LiNbO₃ crystal typically do not exceed few tens of kV/cm[18,20,34] (see also Supplementary Note 5 and Supplementary Fig. 6b, d). Thus, the expected Stark shift due to the out-of-plane acousto-electric effect is below

0.05 meV for the highest RF power $P_{RF} = 26$ dBm (which is the maximum RF power that can be applied to the acoustic transducer without damaging it). This value is two orders of magnitude smaller than the spectral shifts detected in our experiment. However, the Stark tuning coefficient under electric fields applied within the emission dipole plane is still unknown and can lead to larger spectral shifts. A detailed analysis of the optical polarization response of various defect centers (Supplementary Note 6) does not reveal any obvious correlation between the magnitude of the SAW-mediated spectral modulation (ΔE in Fig. 3a) and the orientation of the projection of the transition dipole moment onto the sample plane (measured in Fig. 2b). This is in contrast to the expected similar values of spectral shifts induced by the acousto-electric effect acting on defects with collinear dipole orientations. In fact, we find defects with the same polarization angle and degree showing $\Delta E > 0$ as well as $\Delta E = 0$. Therefore, the contribution of the SAW piezoelectric field (independently of its orientation with respect to the defect symmetry axis) can be neglected in comparison to that induced by the acousto-mechanical effect.

In the presence of the SAW, the ZPL₁ peak in Fig. 3a remains unchanged, therefore indicating that the three peaks (i.e., ZPL₁, ZPL₂ and ZPL₃) probably originate from different emitters with different mechanical coupling strength to the substrate. This assumption is corroborated by the experiments of Fig. 2, which reveal that the characterized emitters exhibit different photophysical properties and temporal dynamics. In fact, the fraction of radiative defects efficiently coupled to the SAW is low (only a few percent). This is probably due to the inhomogeneous shape and size of the dispersed h-BN grains and their random orientation, resulting in an arbitrary mechanical contact between the grains (and thus the embedded emitters) and the underlying substrate. As a matter of fact, only those defects that are contained in heavier grains and are in direct mechanical contact with the substrate are expected to undergo an effective acousto-mechanical modulation. This is consistent with previous findings showing that the amount of strain transfer from the bottom to the top layer in a multilayer h-BN flake[6], or other 2D structures[35], can be strongly limited by the weak interlayer van der Waals interactions. The assumption that the acoustic coupling strength depends on the quality of the

mechanical contact between the emitting state and the vibrating substrate is also corroborated by our recent SAW experiments performed on a similar LiNbO$_3$ SAW-chip accommodating few-layer h-BN flakes deposited on a SAW propagation path. In this case, no effect of the acoustic waves on the defect centers has been observed. Similar behavior was reported for randomly dispersed dot-in-a-nanowire semiconductor heterostructures subjected to a SAW propagating on the surface of a LiNbO$_3$ substrate[20,33]. In these samples, the strongest acoustic coupling of a QD embedded inside a "pencil-like" nanowire top region was observed in nanowires whose pyramidal tip was in direct mechanical contact with the underlying SAW substrate[20]. In addition, in this sample, depositing a thin SiO$_2$ layer over of the randomly dispersed nanowires improves the mechanical coupling between the acoustic substrate and the embedded QDs. As a result, all nanowire QDs probed by optical excitation and subjected to the propagating SAW experience significant SAW-mediated spectral tuning, independently of the nanowire orientation (unpublished result). We expect to observe the same effect in the case of h-BN grains.

Quantification of acousto-mechanical effect. The measured acousto-mechanical response of the excited-state emission intensity ($I(E)$ in Eq. (1)) is quantified by fitting (red dashed traces in Fig. 3a) the SAW-split PL signal (black solid data traces acquired at $P_{RF} = 26$ dBm) to the time-averaged (over $T_{SAW} = 1/f_{SAW}$) Gaussian peak function of constant linewidth w and intensity A given by:

$$I(E) = I_0 + \frac{1}{T_{SAW}} \cdot \frac{A}{w \cdot \sqrt{\frac{\pi}{2}}} \cdot \int_0^{T_{SAW}} e^{-2\frac{(E-E_C(t))^2}{w^2}} dt. \quad (1)$$

Here, $E_C(t)$ is the time-varying emission energy following a sinusoidal temporal evolution with modulation amplitude $\Delta E/2$ around its unperturbed position E_0 [22,34]:

$$E_C(t) = E_0 + \frac{\Delta E}{2} \cdot \sin\left(\frac{2\pi}{T_{SAW}} \cdot t\right). \quad (2)$$

As shown in Fig. 3a, this characteristic line shape matches very well with the measured spectra, thereby allowing to accurately extract the amplitude $\Delta E/2$ of the dynamic spectral modulation.

Figure 4a shows time-integrated PL spectra of the ZPL$_3$ emission line plotted in false-color scale as a function of the acoustic amplitude at the surface of the LiNbO$_3$ substrate. The magnitude of the SAW-induced splitting $\Delta E = E_{max} - E_{min}$ increases with increasing the SAW amplitude ($\propto \sqrt{P_{RF}}$). These findings indicate that the SAWs can be used to effectively fine-tune the emission energy from h-BN defects. The tuning bandwidth reaches up to ~2.5 meV, depending on the emission center. The fitted values of the spectral modulation bandwidth ΔE are plotted in Fig. 4b in a double-logarithmic representation as a function of the acoustic amplitude. Because the strain scales linearly with the acoustic amplitude (which is directly proportional to the square root of the RF power, $\sqrt{P_{RF}}$), we expect that $\Delta E \propto \sqrt{P_{RF}}$.

The linear fits (solid lines) in Fig. 4b yield different strain dependences at low and high SAW amplitudes. From the observed slopes, we identify a power-law dependence ($\Delta E \propto (\sqrt{P_{RF}})^n$) with exponent n equal to 0.97 ± 0.01 (close to expected linear) for low and 0.27 ± 0.01 (non-linear trend) for high acoustic excitation. The non-linearities at large modulation amplitudes may be due to (partial) decoupling of the dispersed h-BN grains from the surface of a LiNbO$_3$ substrate. Such effect may arise from, for example, slight grain rotation or crystallite slippage among the layers composing the host h-BN grain[6,36]. This hypothesis is supported by the observation of an irreversible reduction or even loss of the

SAW-induced PL line splitting for some of the probed defects, whose unperturbed emission spectrum, as well as dipole orientation, remains unchanged. In addition, non-linear and non-monotonic behavior of the ZPL transition energy under the effect of static strain has been suggested for h-BN layers hosting a N$_B$V$_N$ defect[6,7]. Nonetheless, the latter effects are expected to take place at much larger strain values than those used in our experiments (see below). The observed behavior also supports the argument for negligible contribution of the acousto-electric modulation mechanism induced by the SAW piezoelectric field. This is because, even after mechanical decoupling from the substrate, the probed defect (which still maintains the same dipole orientation) is still within the reach of the SAW piezoelectric field and, as such, should still be prone to the acousto-electric modulation. This, however, is not the case here.

Figure 4a displays the fitted ΔE values as a function of the amplitude of the hydrostatic strain induced by the applied SAW at the surface of the LiNbO$_3$ substrate. To determine the magnitude of hydrostatic strain acting on a defect center, we relate the mechanical deformation to the SAW amplitude using numerical model described in ref. [31] and discussed in Supplementary Note 5. For SAW propagating on the surface of a LiNbO$_3$ crystal, the SAW strain field possesses three non-vanishing strain components ϵ_{XX}, ϵ_{ZZ} and ϵ_{XZ} in the reference frame with main crystal axes (defined in Fig. 1a). At the acoustic phase marked with E_{min} (E_{max}) in Fig. 4 corresponding to the minimum (maximum) transition energy, the shear component ϵ_{XZ} vanishes and the hydrostatic strain s_0 consists only of a tensile (compressive) component ϵ_{XX} along the SAW propagation direction (i.e., x-direction) plus a smaller compressive (tensile) component ϵ_{ZZ} in the direction perpendicular to the substrate surface (i.e., z-direction): $s_0 = \epsilon_{XX} + \epsilon_{ZZ}$. This results in the hydrostatic strain on the LiNbO$_3$ surface of the order of $s_0 \approx 0.04\%$ for the highest acoustic amplitude (Supplementary Fig. 6a). Thus, assuming that most of the strain is transferred from LiNbO$_3$ to the h-BN grain on top of it and neglecting the contribution from the SAW piezoelectric field, we evaluate a lower limit of the absolute deformation potential for the h-BN of about 5 eV. This value (which is determined as the ratio of the energy shift ΔE of a given state under strain and the relative change of volume given by the hydrostatic strain s_0[37]) is in accordance with the density functional theory (DFT) estimates presented in refs. [37,38].

Moreover, the linear fit to the experimental data in the lower panel of Fig. 4b shows that the SAW-mediated energy shift of the defect emission in h-BN is of the order of 50 meV/% of strain. This tuning coefficient is in accordance with strain-induced exciton shifts observed for other 2D semiconductors, such as MoS$_2$[39] and WSe$_2$[40], where static strains of 3% result in ~100 meV spectral shifts. The here estimated 50 meV/% tunability is also consistent with the DFT simulation, reported in ref. [7], of the changes imposed by biaxial strain on the optical transition energy in an h-BN monolayer containing a nitrogen-anti-site defect. In this calculation (see also Supplementary Note 7), the spectral changes anticipated for the range of strain values used in our experiment give a smaller value of the strain-tuning coefficient of ~24 meV/%. Our result is, however, an order of magnitude larger than the maximum strain-tuning coefficient of ~6 meV/% found experimentally in multilayer h-BN flakes under externally applied static strain[6]. This is probably due to better quality of the physical contact between the grain hosting the emitting defect and the vibrating substrate. In addition, the aforementioned decoupling of defects from the deformed substrate at large strain values reported in refs. [6,7] (which are orders of magnitude larger than those used in our experiments) could also play a role.
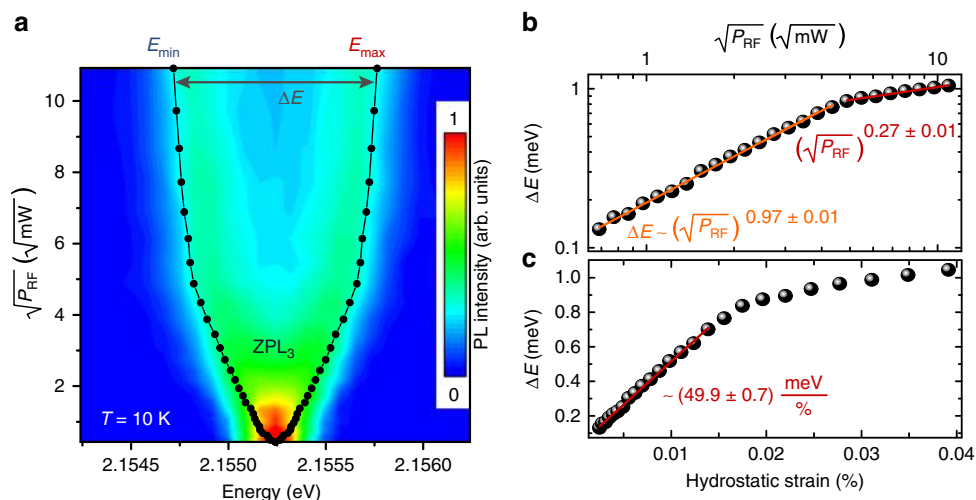
Fig. 4 Acoustic tuning of hexagonal boron nitride (h-BN) optical emission. a False-color plot of the time-integrated low-temperature emission from a single h-BN defect corresponding to zero-phonon line ZPL_3 as a function of the driving surface acoustic wave (SAW) amplitude ($\propto \sqrt{P_{RF}}$), showing the splitting of the optical transition into a doublet consisting of the lowest (E_{min}) and the highest (E_{max}) energy values separated by $\Delta E = E_{max} - E_{min}$. The E_{min} and E_{max} values, extracted from fitting Eq. (1) to the experimental results recorded at different radio-frequency (RF) powers, are indicated by black dots. Energy splitting ΔE as a function of **b** the driving SAW amplitude and **c** the SAW-induced hydrostatic strain at the lithium niobate substrate surface. The solid lines are: power fits to the experimental data in **b** reproducing the $\Delta E \propto (\sqrt{P_{RF}})^n$ dependence and a linear fit to the data shown in **c**
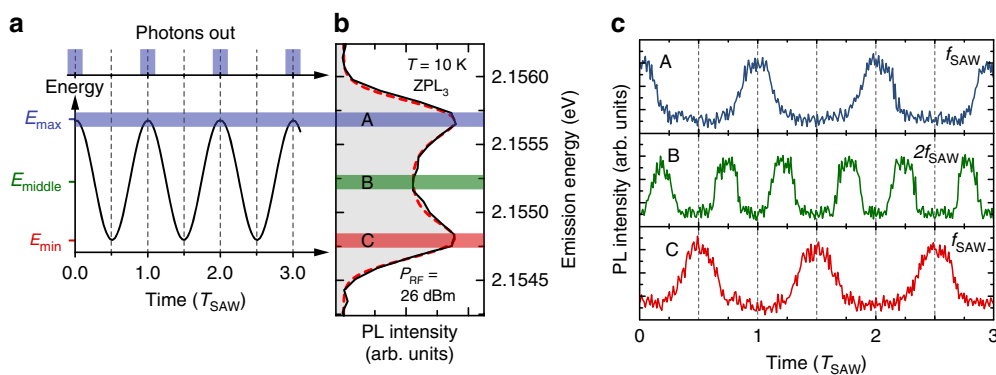
Fig. 5 Photon time-binning via spectral filtering of the surface acoustic wave (SAW)-driven emission wavelength modulation. a Sketch of the sinusoidal temporal modulation of the emission energy (black solid line) of a hexagonal boron nitride defect. The horizontal blue rectangle plotted on top of the sinusoidal spectral tuning depicts the energy window over which photons are collected. The vertical blue rectangles labeled "photons out" outline the temporal emission profile for the selected spectral detection window. **b** Time-averaged photoluminescence spectrum of the SAW-split zero-phonon line ZPL_3. The three superimposed horizontal color-coded rectangles mark the energy regions used for spectral filtering. The red dashed line designates the fit using Eq. (1). **c** The three traces (A, B and C) represent the time-dependent luminescence (in units of the SAW period) spectrally filtered at energies indicated by the corresponding horizontal color-coded rectangles in **a**

Such high elastic response of h-BN allows for effective strain engineering of its optical properties, which is particularly important for implementations of this material into existing photonic and optoelectronic devices. The same effect can, in principle, also explain the giant spectral spread of embedded quantum emitters, which is typically observed in the PL spectra of h-BN[6,7,9–13]. The large strain-driven spectral variability demonstrated here suggests that defects in h-BN can indeed couple to local lattice strain inducing large variations of their emission wavelength.

Strain tuning of the photon emission rate. The SAW-driven dynamic modulation of the defect optical transition can further be used to control the photon emission time. As illustrated in Fig. 5a, this was achieved by collecting the photons in a narrow spectral window. The light (trace labeled A in Fig. 5b) filtered at

the highest energy (blue horizontal rectangle in Fig. 5a) is out of phase with that (trace C in Fig. 5b) filtered at the lowest energy (red rectangle in Fig. 5b), with both oscillating at the SAW frequency. On the contrary, at the central wavelength (green horizontal rectangle in Fig. 5b) the emission occurs at twice the frequency of the SAW (trace B in Fig. 5b), since the emitting state moves past this energy twice per SAW cycle.

In this way, as previously reported for semiconductor QDs in III-nitride[33] and III-arsenide[32] material systems, the photon emission rate and its temporal output profile can be acoustically regulated. Higher repetition rates, which are required for future high-speed quantum information processing can, in principle, be achieved by increasing the acoustic frequency (up to a GHz range). These results also indicate that the photon emission wavelength can be filtered out by time gating of the acoustically governed luminescence from h-BN defects. The latter can be

beneficial for reducing the wavelength variability between different defect centers emitting within the SAW-driven spectral modulation bandwidth. In general, large bandwidths can be reached using higher strain values.

Discussion

In summary, we have studied the effect of SAWs on highly linearly polarized non-classical light emitted from defect centers in h-BN grains. We show that the electronic transitions in optically probed h-BN grains are sensitive to the strain of propagating acoustic waves, and that this can be used as an efficient tool for in situ simultaneous control of the photon emission wavelength as well as their emission time. Like in other solid-state systems[21,22,32,33], the dynamic strain provides an effective method to control the optical properties of embedded quantum emitters in h-BN. As a more general view, the ability to induce spectral shifts up to 50 meV per strain percentage is beneficial for overcoming the spectral inhomogeneity of atomic defects in h-BN.

Moreover, the dynamically tuned photon emission can be combined with the real-time-gating functionality, therefore facilitating the production of energetically identical defect-related quantum emitters. Altogether, our results present an important advance towards controlling the emission properties of defects in h-BN via strain engineering, with important practical implications in quantum communication and photonic quantum information processing.

Methods

Optical characterization. For the low-temperature optical spectroscopy experiment, the sample was placed in vacuum in a Helium-flow cold finger cryostat. For time-integrated PL measurements, the h-BN grains were excited by a linearly polarized continuous-wave 532 nm excitation laser source. The laser beam was focused to a 1.5 μm spot onto the sample by a ×50 microscope objective lens (NA = 0.73). The emitted light was collected by the same objective lens, passed through a 532-nm ultrasteep long-pass edge filter, dispersed by a single-grating monochromator (with spectral resolution of ~250 μeV) and detected with a liquid nitrogen-cooled CCD camera. In the $g^{(2)}(\tau)$ measurements, the luminescence peak of interest was filtered by the same monochromator and directed to a HBT interferometer mounted on the monochromator's side exit. The HBT setup consists of two avalanche photo-diodes (APDs from Perkin Elmer) positioned in the transmission and reflection arm of a 50:50 non-polarizing beam-splitter cube and connected to a time-correlated single-photon counting module (PicoHarp, Picoquant). An additional 650-nm short-pass filter was placed in front of one of the APDs to eliminate the effect of afterpulsing in the autocorrelation. The same setup with only one APD was used for time-resolved PL measurements under pulsed excitation with 442 nm wavelength, <100 ps pulse width and 40 MHz repetition rate. For polarization-dependent measurements, an achromatic half-wave-plate and a beam-displacing prism with two orthogonally polarized outputs were inserted in the optical collection path. The use of a fixed polarization analyzer and of a quarter-wave-plate added in front of the monochromator's entrance slit eliminates the effects of the polarization anisotropy of the diffraction grating. The excitation polarization orientation was fixed along the SAW propagation direction, which was aligned with the spectrometer's entrance slit and which also corresponds to the extraordinary transmission axis of the beam-displacing prism. The projection of the emission dipole onto the sample plane (i.e., the in-plane angle information in Fig. 2b) and the degree of polarization were determined by rotating the retardation waveplate between 0° and 180° in steps of 5°, with 0° denoting the SAW propagation direction (i.e., x-axis in Fig. 1).

Sample fabrication. The SAW-chip was fabricated on a commercial 128° Y-cut LiNbO₃ substrate. Two IDTs (35 finger pairs), forming the SAW delay line, were patterned by photolithography and finalized in a lift-off metallization process (10 nm Ti/30 nm Al/10 nm Ti). Thermally expanded hexagonal BN powder was mechanically transferred to the region between the two IDTs on the SAW-chip. A full characterization of the acoustic transducers was performed at room temperature by measuring the RF reflection and transmission spectra using a vector network analyzer (not shown). From these analyses, we determined an electric to acoustic power conversion efficiency of ~30% for both transducers (see ref. [18] for more information). Thus, only 30% of the nominal power applied by the RF signal generator is converted into acoustic power. This efficiency was constant over the full RF power range used in the experiments. In order to discriminate between the SAW effects from those induced by heating of the sample at high RF powers, the laser excitation and the RF signal were chopped at the same frequency of 400 Hz[41]. To eliminate the temperature-induced effects, for each acoustic power, the PL

spectrum recorded for the optical and RF excitations out-of-phase (only thermal effects) was subtracted from that measured for the in-phase condition (SAW plus thermal effects). This procedure becomes particularly important for the determination of the small spectral shifts (smaller than the characteristic PL linewidths) induced by the SAW fields. No significant RF-induced thermal contribution on the ZPL position and intensity was detected.

Data availability

The data that support the findings of this study are available from the corresponding author on reasonable request.

References

1. Lounis, B. & Orrit, M. Single-photon sources. *Rep. Prog. Phys.* **68**, 1129–1179 (2005).
2. Aharonovich, I., Englund, D. & Toth, M. Solid-state single-photon emitters. *Nat. Photon.* **10**, 631–641 (2016).
3. Bourrellier, R. et al. Bright UV single photon emission at point defects in h-BN. *Nano Lett.* **16**, 4317–4321 (2016).
4. Martínez, L. J. et al. Efficient single photon emission from a high-purity hexagonal boron nitride crystal. *Phys. Rev. B* **94**, 121405 (2016).
5. Chejanovsky, N. et al. Structural attributes and photodynamics of visible spectrum quantum emitters in hexagonal boron nitride. *Nano Lett.* **16**, 7037–7045 (2016).
6. Grosso, G. et al. Tunable and high-purity room temperature single-photon emission from atomic defects in hexagonal boron nitride. *Nat. Commun.* **8**, 705 (2017).
7. Tran, T. T. et al. Robust multicolor single photon emission from point defects in hexagonal boron nitride. *ACS Nano* **10**, 7331–7338 (2016).
8. Tran, T. T., Bray, K., Ford, M. J., Toth, M. & Aharonovich, I. Quantum emission from hexagonal boron nitride monolayers. *Nat. Nanotechnol.* **11**, 37–41 (2016).
9. Jungwirth, N. R. et al. Temperature dependence of wavelength selectable zero-phonon emission from single defects in hexagonal boron nitride. *Nano Lett.* **16**, 6052–6057 (2016).
10. Jungwirth, N. R. & Fuchs, G. D. Optical absorption and emission mechanisms of single defects in hexagonal boron nitride. *Phys. Rev. Lett.* **119**, 057401 (2017).
11. Tran, T. T. et al. Quantum emission from defects in single-crystalline hexagonal boron nitride. *Phys. Rev. Appl.* **5**, 034005 (2016).
12. Koperski, M., Nogajewski, K. & Potemski, M. Single photon emitters in boron nitride: more than a supplementary material. *Opt. Commun.* **411**, 158–165 (2018).
13. Ziegler, J. et al. Single-photon emitters in boron nitride nanococoons. *Nano Lett.* **18**, 2683–2688 (2018).
14. Noh, G. et al. Stark tuning of single-photon emitters in hexagonal boron nitride. *Nano Lett.* **18**, 4710–4715 (2018).
15. Golter, D. A. et al. Coupling a surface acoustic wave to an electron spin in diamond via a dark state. *Phys. Rev. X* **6**, 041060 (2016).
16. Golter, D. A., Oo, T., Amezcua, M., Stewart, K. A. & Wang, H. Optomechanical quantum control of a nitrogen-vacancy center in diamond. *Phys. Rev. Lett.* **116**, 143602 (2016).
17. Whiteley, S. J. et al. Spin–phonon interactions in silicon carbide addressed by Gaussian acoustics. *Nat. Phys.* **15**, 490–495 (2019).
18. Hernández-Mínguez, A. et al. Acoustically driven photon antibunching in nanowires. *Nano Lett.* **12**, 252–258 (2012).
19. Weiß, M. et al. Radio frequency occupancy state control of a single nanowire quantum dot. *J. Phys. D* **47**, 394011 (2014).
20. Lazić, S. et al. Dynamic control of the optical emission from GaN/InGaN nanowire quantum dots by surface acoustic waves. *AIP Adv.* **5**, 097217 (2015).
21. Pustiowski, J. et al. Independent dynamic acousto-mechanical and electrostatic control of individual quantum dots in a LiNbO3-GaAs hybrid. *Appl. Phys. Lett.* **106**, 013107 (2015).
22. Nysten, E. D. S. et al. Multi-harmonic quantum dot optomechanics in fused LiNbO₃–(Al)GaAs hybrids. *J. Phys. D* **50**, 43LT01 (2017).
23. Kinzel, J. B. et al. The native material limit of electron and hole mobilities in semiconductor nanowires. *ACS Nano* **10**, 4942–4953 (2016).
24. Hernández-Mínguez, A., Lähnemann, J., Nakhaie, S., Lopes, J. M. J. & Santos, P. V. Luminescent defects in a few-layer h-BN film grown by molecular beam epitaxy. *Phys. Rev. Appl.* **10**, 044031 (2018).
25. Vogl, T., Campbell, G., Buchler, B. C., Lu, Y. & Lam, P. K. Fabrication and deterministic transfer of high-quality quantum emitters in hexagonal boron nitride. *ACS Photon.* **5**, 2305–2312 (2018).

26. Proscia, N. V. et al. Near-deterministic activation of room-temperature quantum emitters in hexagonal boron nitride. *Optica* **5**, 1128–1134 (2018).

27. Kurtsiefer, C., Mayer, S., Zarda, P. & Weinfurter, H. Stable solid-state source of single photons. *Phys. Rev. Lett.* **85**, 290–293 (2000).

28. Shotan, Z. et al. Photoinduced modification of single-photon emitters in hexagonal boron nitride. *ACS Photon.* **3**, 2490–2496 (2016).

29. Weston, L., Wickramaratne, D., Mackoit, M., Alkauskas, A. & Van de Walle, C. G. Native point defects and impurities in hexagonal boron nitride. *Phys. Rev. B* **97**, 214104 (2018).

30. Santos, P. V., Alsina, F., Stotz, J. A. H. & Hey, R. Band mixing and ambipolar transport by surface acoustic waves in GaAs quantum wells. *Phys. Rev. B* **69**, 155318 (2004).

31. de Lima, M. M. Jr. & Santos, P. V. Modulation of photonic structures by surface acoustic waves. *Rep. Prog. Phys.* **68**, 1639–1701 (2005).

32. Gell, J. R. et al. Modulation of single quantum dot energy levels by a surface-acoustic-wave. *Appl. Phys. Lett.* **93**, 081115 (2008).

33. Lazić, S., Hernández-Mínguez, A. & Santos, P. V. Control of single photon emitters in semiconductor nanowires by surface acoustic waves. *Semicond. Sci. Technol.* **32**, 084002 (2017).

34. Lazić, S., Chernysheva, E., Hernández-Mínguez, A., Santos, P. V. & van der Meulen, H. P. Acoustically regulated optical emission dynamics from quantum dot-like emission centers in GaN/InGaN nanowire heterostructures. *J. Phys. D* **51**, 104001 (2018).

35. Kumar, H., Dong, L. & Shenoy, V. B. Limits of coherency and strain transfer in flexible 2D van der Waals heterostructures: formation of strain solitons and interlayer debonding. *Sci. Rep.* **6**, 21516 (2016).

36. Balima, F. et al. Shear effects on expanded graphite under uniaxial pressure: an in situ small angle neutron scattering study. *Carbon* **74**, 54–62 (2014).

37. Wiktor, J. & Pasquarello, A. Absolute deformation potentials of two-dimensional materials. *Phys. Rev. B* **94**, 245411 (2016).

38. Bruzzone, S. & Fiori, G. Ab-initio simulations of deformation potentials and electron mobility in chemically modified graphene and two-dimensional hexagonal boron-nitride. *Appl. Phys. Lett.* **99**, 222108 (2011).

39. Castellanos-Gomez, A. et al. Local strain engineering in atomically thin MoS$_2$. *Nano Lett.* **13**, 5361–5366 (2013).

40. Desai, S. B. et al. Strain-induced indirect to direct bandgap transition in multilayer WSe$_2$. *Nano Lett.* **14**, 4592–4597 (2014).

41. Camacho, J. et al. Modulation of the electronic properties of GaN films by surface acoustic waves. *J. Appl. Phys.* **94**, 1892–1897 (2003).

42. Reich, S. et al. Resonant Raman scattering in cubic and hexagonal boron nitride. *Phys. Rev. B* **71**, 205201 (2005).

Acknowledgements

Author contributions

Additional information